

Impact of the tropopause temperature on the intensity of tropical cyclones – an idealized study using a mesoscale model

Shuguang Wang¹, Suzana J. Camargo², Adam H. Sobel^{1,2,3}, and Lorenzo M. Polvani^{1,2,3}

¹ Department of Applied Physics and Applied Mathematics, Columbia University, New York, NY

² Lamont-Doherty Earth Observatory of Columbia University, Palisades, NY

³ Department of Earth and Environmental Sciences, Columbia University, New York, NY

Submitted to the Journal of Atmospheric Sciences

2014

Corresponding author: Shuguang Wang, Department of Applied Physics and Applied Mathematics,
Columbia University, New York, NY 10025, sw2526@columbia.edu

2 **Abstract**

3
4 This study investigates the impact of the tropopause temperature on the intensity of idealized
5 tropical cyclones (TCs) superimposed on background states of radiative-convective equilibrium
6 (RCE) in a 3D mesoscale model. Simulations are performed with constant sea surface temperature,
7 and an isothermal stratosphere with constant tropopause temperature. The potential intensity (PI)
8 computed from the thermodynamic profiles of the RCE state (before the TCs are superimposed on it)
9 increases 0.4 to 1 m/s for each degree of tropopause temperature reduction. The 3D TC experiments
10 yields intense tropical cyclones whose intensities exceed the PI value substantially. It is further
11 shown that the discrepancy may be largely explained by the super-gradient wind in the 3D
12 simulation. The intensity of these 3D TCs shows a ~ 0.4 m/s increase with one degree cooling in the
13 tropopause temperature in RCE, on the lower end of the PI dependence on the tropopause
14 temperature. Sensitivity experiments with larger horizontal grid spacing 8 km produce less intense
15 TCs, as expected, but similar dependence (~ -0.5 m/s/K) on tropopause temperature. Equilibrium
16 TC solutions are further obtained in 200-day experiments with different values of constant
17 stratospheric temperature. Similar relationships between TC intensity and tropopause temperature
18 are also found in these equilibrium TC solutions. It is shown that a colder tropopause not only
19 yields more intense TCs, but also leads to larger temporal variability in the TC intensity.

20

21 **1. Introduction**

22 The cooling trend in the tropical lower stratosphere is one of the most dramatic climate
23 change signals in the recent climate record (Randel et al. 2009, Emanuel et al. 2013, Vecchi et al.
24 2013). Recent studies (Emanuel 2010, Emanuel et al. 2013, Vecchi et al. 2013) have shown
25 evidence that this stratospheric temperature trend near the tropopause may have influenced tropical
26 cyclone (TC) activity in the tropical North Atlantic basin. These recent results provide motivation to
27 study the influence of thermodynamic conditions in the upper troposphere and lower stratosphere on
28 TCs in more detail.

29 Potential intensity theory (Emanuel references) models TCs as heat engines, operating
30 between the warm ocean and the cold tropopause and converting thermal energy to mechanical
31 energy. Variations in the sea surface temperature (SST) have received much attention in the
32 literature (e.g., Vecchi and Soden 2007, Ramsay and Sobel 2011). The effect of temperature near
33 the tropopause has been less thoroughly studied. It is often assumed that the TC outflow
34 temperature is directly set by the ambient tropopause temperature via gravity wave adjustment.
35 Recent developments of the TC theory (Emanuel and Rotunno, 2011, Emanuel 2012), however,
36 suggests that this conventional view of the TC outflow is incomplete. In these recent studies, the
37 criticality of the Richardson number in the outflow is found to be a strong constraint on the
38 stratification of the outflow temperature, which sets the radial distribution of the wind speed
39 through moist adjustment.

40 Emanuel (2010, 2011) provided observational evidence that temperature variations in the
41 stratosphere have contributed to the interannual variability of the TC potential intensity in the last
42 30 years. Yet, because of well-known observational issues, tropical temperatures in the upper
43 troposphere and lower stratosphere in the reanalysis data sets (e.g., ERA and NCEP) are uncertain
44 (Vecchi et al, 2013). Perhaps equally importantly, the impact of temperature at these levels on TC
45 intensity is difficult to assess from observations.

46 Another line of evidence for the importance of the tropopause temperature comes from
47 global climate models (Vecchi et al 2013) that can faithfully simulate interannual variability of TC
48 activity (Zhao et al. 2009, Zhao and Held 2012) as well as regional downscaling systems designed
49 for similar objectives (Knutson et al. 2008). Vecchi et al. (2013) also showed that the North Atlantic
50 TC activity simulated by a high-resolution climate model and a regional TC downscaling system is
51 modulated by changes in temperature in the upper troposphere/lower stratosphere (UT/LS) region,
52 although the effect is weaker than in Emanuel's studies.

53 Several axisymmetric modeling studies have documented the effect of the outflow
54 temperature on simulated TC intensity (Rotunno and Emanuel 1987, Mrowiec and Pauluis 2011,
55 Emanuel and Rotunno 2011, Ramsay 2013). Ramsay (2013) compared the effect of the tropopause
56 temperature to SST in an idealized axisymmetric model, and found that one degree warming in SST
57 can change the potential intensity (PI) by 2 m/s while one degree decrease in the tropopause
58 temperature increases PI by 1 m/s. Because the UT/LS temperature has larger natural variability
59 than SST and the latter is ultimately limited by the thermal inertia of the ocean, this suggests that, as
60 also noted in Emanuel (2011), the tropopause temperature may have played a more important role
61 than SST in the TC intensity.

62 While much about TC-environment interaction has been learned using axisymmetric models
63 (e.g., Ooyama 1969, Rotunno and Emanuel 1987, Craig and Gray 1996, Persing et al. 2003,
64 Hausman et al. 2006, Bryan et al 2009a ,b, Mrowiec et al. 2011, Hakim 2011, Emanuel and
65 Rotonno 2013), several recent studies (e.g., Yang et al. 2007; Persing et al. 2013) have
66 demonstrated that ignoring asymmetric dynamics may lead to overestimates of TC intensity,
67 suggesting that explicitly resolved three-dimensional TC structure and convective eddies may be
68 important for studying TC-environment interaction. In this work, we use a 3D, full-physics
69 mesoscale model to: (1) examine the effect of the tropopause temperature on hurricane intensity,

70 and (2) further compare the predictions of potential intensity theory to the results of 3D modeling
71 experiments.

72 The rest of this paper is organized as follows. Section 2 contains a description of the
73 numerical experiments, followed by the results of transient TC solutions in Section 3 and
74 equilibrium TC solutions in Section 4. Section 5 summarizes the results.

75 **2. Experiment design**

76 We perform numerical experiments of idealized tropical cyclones developed from a finite
77 amplitude vortex. The initial vortex is the same as that specified in Rotunno and Emanuel (1987).
78 This is an idealized moist warm core vortex in gradient and hydrostatic balance, with the maximum
79 wind speed at the surface. The warm core structure differs from the observed cold cores typically
80 found during early phases of TC genesis (Bister and Emanuel 1997, Raymond et al., 2007). Because
81 of this, the subsequent development of the initial vortex does not represent the transition from the
82 warm to cold core, as in some other studies (e.g, Montgomery et al. 2006, Rappin et al. 2010).
83 Nevertheless, this warm core vortex initialization suffices for our purpose, since the present study
84 focuses on the intensity of the mature TC.

85 The environment into which the TC vortex is introduced by the soundings from an RCE
86 simulation in a small domain, similar to the procedure in Nolan et al. (2007). A distinct advantage
87 of using a RCE sounding is that the environment is already close to equilibrated before the TC is
88 introduced. While the presence of the TC itself can change the mean state, the effect of any initial
89 shock from disequilibrium in the environment itself (apart from the TC's own influence) on the TC
90 solution is small. This is desirable in a study of the influence of the environment on TC intensity.

91 The Advanced Research Weather Research and Forecasting (WRF) model version 3.0
92 (Skamarock et al. 2008) is used for this study. The radiation package is replaced by a Newtonian
93 cooling scheme (Pauluis 2006, Wang and Sobel 2011),

$$94 \quad Q|_{rad. \ cooling} = \begin{cases} -1.2 \text{ K} \cdot \text{day}^{-1} & \text{for } T > 6 + T_o \\ -\frac{T - T_o}{5 \text{ days}} & \text{for } T \leq 6 + T_o \end{cases} \quad (1).$$

95 With this simple treatment of radiation, the troposphere is cooled at a constant rate of 1.2 K/day,
 96 which is close to the observed climatology of net radiative cooling, and stratospheric temperature is
 97 relaxed to a constant T_o . T_o is used as the control parameter for the numerical experiments in this
 98 study.

99 The RCE is computed on a double-periodic numerical domain of $200 \times 200 \times 23 \text{ km}^3$ at
 100 horizontal grid spacing $Dx = 4 \text{ km}$ with a given a SST and T_o . The Coriolis parameter $f = 0.5 \times 10^{-4}$
 101 s^{-1} . Using the RCE solution to define the initial state, we then perform two types of TC simulations:
 102 short term (~ 10 days) simulations designed to identify the peak TC intensity obtainable with a
 103 given environment, and long term (~ 200 days) ones to obtain equilibrium TC solutions. **Table 1**
 104 summarizes all the numerical experiments. Two computational domains are used in the transient TC
 105 integrations: a large one ($6000 \times 6000 \times 26 \text{ km}^3$) with grid spacing $Dx = 12 \text{ km}$, and a smaller one
 106 ($1200 \times 1200 \times 26 \text{ km}^3$) in the middle of the large one, with grid spacing $Dx = 4 \text{ km}$. Double
 107 periodic boundary conditions are adopted for the outer domain. 50 vertical levels are used with
 108 stretched vertical level spacing. The computational domain in the equilibrium TC integrations uses
 109 only one grid ($3200 \times 3200 \times 26 \text{ km}^3$) with $Dx = 8 \text{ km}$. The nominal model top of all numerical
 110 grids is set to 26 km.

111 We vary the tropopause temperature T_o in Equation (1) from 195 K to 215 K in increments
 112 of 5K. This range is larger than that derived from either the NCEP/NCAR or ERA40 reanalysis
 113 datasets from the late 1970s to 2002, but is intended to bracket the observationally-derived range.
 114 The mean soundings from the RCE integrations with these T_o values and SST set to 28°C are shown
 115 in Figure 1. The largest difference in temperature among these soundings occurs at the tropopause

116 level and the stratosphere, and becomes smaller in the lower troposphere for both temperature and
117 humidity.

118 Besides the simple treatment of radiative cooling, the following physics schemes are used
119 for both the small domain RCE and large domain TC integrations. Boundary layer turbulence and
120 vertical transport by subgrid eddies are parameterized using the Yonsei University (YSU) scheme
121 (Hong et al., 2006); horizontal transport by subgrid eddies is treated using Smagorinsky first order
122 closure; the surface moisture and heat fluxes are parameterized following Monin-Obukhov
123 similarity theory, together with Charnock relationship for the surface roughness; and the Purdue-Lin
124 scheme is used for cloud microphysics (Lin et al. 1983). The horizontal and vertical advection
125 schemes are 5th order and 3rd order accurate, respectively. Moisture and condensate are advected
126 using a positive definite scheme. We use the implicit damping scheme to suppress unphysical
127 reflection of vertically propagating gravity waves in the top 5 km of the numerical grid (Klemp et al.
128 2008). We adopted these physical schemes partly because we have found that both domain-
129 averaged moisture and moist static energy are better conserved with this particular parametrization
130 choices than with others (not shown). Convective parameterization is not used in any numerical
131 experiment in this study.

132 The following paragraph contains some technical details that have significant implications
133 for our TC integrations, but may be skipped for uninterested readers. The YSU boundary layer
134 scheme parameterizes not only boundary layer eddies but also free tropospheric turbulent eddies,
135 including turbulence onset near the TC outflow regions. Prior studies by Nolan et al (2009) and
136 Kepert (2012) showed that this scheme works reasonably well in the hurricane boundary layer
137 despite its simplicity. Vertical eddy viscosities above the entrainment zone overlaying the mixed
138 layer have a specified dependence on stability and mixing length. The latter varies with height,
139 approaching 30 m in the free troposphere. Horizontal subgrid-scale eddy viscosity is a function of

140 two environmental parameters, horizontal mixing length and flow deformation. The horizontal eddy
141 viscosity coefficient is written as $K_h=(C_s*D_x)^2 S$, where D_x is the horizontal grid spacing, S is flow
142 deformation, and $C_s =0.25$. Thus the mixing length is resolution dependent $l_h = C_s *D_x$, and l_h is 1
143 km in the $D_x = 4$ km integration and 2 km in the $D_x = 8$ km integration. Bryan and Rotunno (2009)
144 have examined the importance of the horizontal mixing length l_h for the TC intensity in
145 axisymmetric models, and shown that 3D turbulent eddies parameterized by mixing length may
146 smooth out the frontal structure near the eye wall region, thus reducing the TC intensity. The
147 vertical eddy viscosity in the free troposphere is a function of the vertical mixing length l_h (30
148 meters), the stability function, and vertical wind shear. Onset of turbulence occurs when the local
149 gradient Richardson number becomes negative. Dissipative heating is not included in this study.
150 Tests with the dissipative heating effect (Bister and Emanuel 1998, Zhang and Altshuler 1999)
151 reveal insignificant changes in the TC intensity in our model. While Bister and Emanuel (1998) and
152 other subsequent numerical studies have suggested that the dissipation of kinetic energy at the air–
153 sea interface through molecular diffusion may boost the TC intensity, a recent observational study
154 by Zhang (2010) suggested that the effect of dissipative heating may be smaller by a factor of 3 than
155 the formulation in Bister and Emanuel (1998). We do not pursue this issue further in this study.

156 Because of their highly axisymmetric structure, TCs are most conveniently studied in
157 cylindrical coordinates. We use the following procedures to convert the 3D model fields from the
158 Cartesian to cylindrical coordinates: (1) find the maximum and minimum values of surface pressure,
159 and calculate contours of surface pressure whose values lie within 30% and 70% of the range of the
160 surface pressure; (2) fit each of the contours of surface pressure to an ellipse using least squares,
161 and use the geometric center of these ellipses as the origin of the cylindrical coordinates; (3)
162 interpolate 3D fields from Cartesian to cylindrical coordinates. This method yields higher
163 maximum axisymmetric wind speeds by as much as 30% compared to alternative methods using

164 either minimum sea level pressure or maximum vorticity as the origin, which may reduce maximum
165 azimuthal wind speed due to aliasing of low wavenumber features.

166 3. Results

167 3.1 PI from radiative-convection equilibrium

168 The potential intensity (PI) expressed as the maximum wind speed V , can be written as:

$$169 \quad V^2 = \frac{C_k}{C_d} \frac{T^s - T^o}{T^o} (k^* - k), \quad (2)$$

170 where V is given in meters per second; C_k and C_d are the heat exchange and the drag coefficient,
171 respectively; T^o is outflow temperature; T^s is sea surface temperature; k^* is the ocean surface
172 enthalpy; and k is the near surface air enthalpy. This expression states that PI should be a nonlinear
173 function of the outflow temperature T^o . A more accurate expression for PI (Bister and Emanuel
174 2002), derived from energy balance within a control volume along the angular momentum surface
175 at the radius of maximum wind (RMW) is used in Emanuel's PI code to compute PI from an
176 environmental sounding:

$$177 \quad V^2 = \frac{C_k}{C_d} \frac{T^s}{T^o} [CAPE^* - CAPE]_M, \quad (3)$$

178 where CAPE is the convective available potential energy of a near surface air parcel in the
179 environmental sounding, while $CAPE^*$ is the same quantity except for an saturated air parcel lifted
180 from sea surface at the RMW. The outflow temperature T^o is the temperature at the level of neutral
181 buoyancy for the rising parcel. Both CAPE and T^o depend on specific thermodynamic assumptions.
182 Uncertainties in several parameters may change the estimate of PI and its dependence on
183 environmental parameters: the value of C_k/C_d , the thermodynamic assumptions used to compute
184 CAPE, and the use of dissipative heating.

185 Figure 2 shows that the PI values computed for from the RCE soundings vary approximately
186 linearly as a function of outflow temperature, at least in the limited range of T^o studied. The outflow

187 temperature (the horizontal axis) obtained from Emanuel's PI code corresponds well to T_o in
188 equation (1).

189 We use two different values of C_k/C_d , 0.5 and 0.9, in the PI code for Fig. 2a and 2b,
190 respectively. In our 3D WRF integrations, C_k and C_d are computed interactively within the model
191 using the Charnock relation in the surface layer parameterization. The computed ratio is ~ 0.9 far
192 from the radius of maximum wind, and ~ 0.4 near RMW. The lower value, 0.4, is yet smaller than
193 the lower bound obtained from recent observational based estimates (0.5 - 0.7) in several recent
194 studies (Black et al. 2007; Haus et al. 2010; Bell et al. 2010; Zhang et al. 2010). Strictly, the
195 derivation of PI is consistent with the use of the value at the RMW, rather than the (here much
196 larger) environmental value. However, in many applications – such as the computation of PI from
197 large-scale observational data sets in situations where no TC exists – it is common to use
198 environmental values. Here, we find that the actual values from the RMW give PI values which
199 significantly underestimate the actual peak TC intensities produced by the model, while the
200 environmental values gives a much better agreement with the TC intensities.

201 We also consider three choices which differ from the default settings used in the PI code:
202 First, the effect of dissipative heating is switched off, because it is not used in our numerical WRF
203 experiments. Second, pseudo-adiabatic rather than reversible adiabatic thermodynamics is used in
204 the computations of CAPE and outflow temperature. The former is more appropriate in the context
205 of the PI theory, as discussed in Bryan and Rotunno (2009). Finally, the reduction factor of surface
206 maximum wind is set to 1 instead of default value of 0.7, since we compare directly to the
207 maximum wind speed above the boundary layer.

208 Varying these PI parameters yields different PI estimates, and consequently different
209 relationships between PI and outflow temperature in the RCE soundings. **Table 2** summarizes the
210 slope from the linear regression between the PI values and T_o for all the RCE soundings, as we use

211 three values of C_k/C_d (0.5, 0.7, and 0.9), either pseudo-adiabatic or reversible thermodynamics, and
212 either dissipative heating or no dissipative heating. The PI value computed from an RCE sounding
213 with SST = 28°C and $T_o = 205\text{K}$ is also shown in the parenthesis of **Table 2**. Because of
214 uncertainties in several adjustable parameters in the formulation of the PI code as discussed above,
215 the estimated PI dependence on the outflow temperature varies considerably. For example, using
216 reversible thermodynamics and dissipative heating yields ~1 m/s increase of PI with 1K cooling at
217 the tropopause. We estimate that the PI dependence on the tropopause temperature falls in the range
218 from -1 to -0.4 m/s/K. We will show that the dependence of the TC intensity on the tropopause
219 temperature from the 3D experiments of TCs is on the lower end of this estimate.

220 **3.2 TC in a RCE environment**

221 **3.2.1 Structure of simulated TCs**

222 In this section, we focus on the temporal and spatial structure of the TCs simulated in the
223 RCE environment using the WRF model. Figure 3 shows the time-radius plot of tangential wind
224 speed and vertical velocity of the TC simulated with SST=28°C and $T_o=205\text{K}$. Both the tangential
225 and vertical winds show that the TC spins up and reaches over 95 m/s after day 3.75, maintains its
226 peak intensity for 1-1.5 days, and decays after day 5. The peak intensity of this transient TC
227 solution greatly exceeds the theoretical maximum wind speed calculated from the PI code, ~59 m/s,
228 if $C_k/C_d \sim 0.5$ at RMM is used, and even significantly exceeds the value of ~80 m/s obtained if the
229 environmental value, $C_k/C_d \sim 0.9$ is used (see Fig. 2, Table 2).

230 Figure 4 displays the azimuthally averaged structure of this TC at its peak intensity. The
231 temperature anomalies maximize in the upper troposphere around 12 km, while cold temperature
232 anomalies due to downdrafts are found near the surface between 25 and 50 km radius. Positive
233 moisture anomalies appear near the RMW due to moisture transport by the strong vertical motion
234 (Figure 4b). Negative moisture anomalies are seen in the lower free troposphere 150 km away from
235 the center, primarily due to descending branch of the secondary flow. Boundary layer inflow (Fig.

236 4d) reaches 35 m/s and outflow in the upper troposphere reaches over 25 m/s. A secondary outflow
237 just above the boundary layer but below the melting layer is evident near the RMW. The azimuthal
238 mean vertical velocity reaches ~6 m/s near the RMW, indicating intense convective activity.

239 Emanuel and Rotunno (2011) showed that the Richardson number R_i reaches a critical value
240 in the outflow region, where the flow is marginally stable; moist neutrality further ensures that this
241 criticality in the upper layer is communicated to the lower levels and sets the radial distribution of
242 the azimuthal wind. Figure 4e shows that R_i , $R_i=N^2/(u_z^2+v_z^2)$, where u_z and v_z is vertical wind shear,
243 and N is the Brunt-Väisälä frequency, for the azimuthally averaged flow is close to zero within a
244 thin layer in the upper troposphere, though it is rarely below its critical value (zero in this model).
245 This is in agreement with Emanuel and Rotunno (2011) to some degree. However, the radial
246 distribution of mean azimuthal wind in the 3D experiments does not closely resemble the theoretical
247 solution in their study. A possible reason might be that the ratio of the enthalpy exchange and drag
248 coefficients, C_k/C_d , taken to be a constant in their theory, varies considerably in the radial direction
249 in our simulations.

250 The maximum azimuthal wind, ~ 99 m/s, is located at the top of the boundary layer (the
251 black curves in Figures 4c and 4d) at ~ 1.3 km. The boundary layer height is diagnosed in the YSU
252 boundary scheme as the level at which the bulk Richardson number reaches its critical value. In the
253 results, it co-varies with the inflow depth in the radial direction. This differs from the boundary
254 layer of a theoretical dry vortex, which decreases monotonically from the far field to the TC eye and
255 scales as $(2K/\Omega)^{0.5}$ (Kerpert 2001, Smith and Vogl 2008), where K is the eddy viscosity in the
256 boundary layer, and Ω is the angular velocity. Since Ω increases inward, the boundary layer
257 thickness decreases according to the above scaling relationship, and the TC flow tends to be more
258 homogeneous, behaving as a solid body rotation. The boundary layer height in Figure 4d also
259 differs from the recent observational study in Zhang et al. (2011). This discrepancy may be

260 explained by the fact (1) the effect of moisture is not considered in the theoretical dry vortex, and (2)
261 that the observed TCs are rarely as strong as those simulated in our numerical study.

262 **3.2.2 Simulated TC intensity and potential intensity**

263 The PI theory (Emanuel, 1987) plays a vital role in the studies of the hurricane-climate
264 connection. It has been tested, to some extent, against observations (Emanuel, 2000; Wing et al.
265 2007; Kossin and Camargo, 2009) and in several numerical studies (e.g., Nolan et al. 2007, Bryan
266 and Rotunno 2009a). It is now well accepted that PI theory offers a reasonable upper bound on
267 balanced axisymmetric TCs. On the other hand, several authors have shown that this upper bound
268 may be regulated by a few factors not considered in the theory: turbulent diffusion in the radial
269 direction (Rotunno and Bryan 2011a), super-gradient wind (Bryan and Rotunno 2009a), intrusion of
270 low entropy air associated with wind shear (Tang and Emanuel 2010, 2012), the highly unbalance
271 flow in the hurricane boundary layer (Smith et al. 2008; Smith and Montgomery 2010), lateral
272 energy transport (Wang and Xu 2010), and cooling of the upper ocean by TC-induced mixing (Lin
273 et al. 2013). However, a more complete theory relating only environmental fields to TC intensity
274 does not exist yet.

275 In the axisymmetric framework, values of maximum azimuthal mean wind (V_{max}) larger than
276 those predicted by PI theory have been found in several modeling studies (Persing and Montgomery
277 2003, Hausman et al. 2006, Yang et al., 2007, Bryan and Rotunno 2009b). Bryan and Rotunno
278 (2009) attributed this large difference between the PI value and the simulated V_{max} from an
279 axisymmetric model partly to gradient flow imbalance – the azimuthal flow at eyewall is highly
280 supergradient – and partly to the turbulent length scale. Comparisons between PI and the results
281 from 3D models have not been made as systematically as have those with axisymmetric models. In
282 idealized numerical experiments of TCs starting from RCE, Nolan et al (2007) found that TC
283 intensities reached about 70% of the PI.

284 We have tested different domain sizes; our results suggest that the small domain size (1200
 285 km) used by Nolan et al. (2007) may constrain the intensity of the TCs. As we increase our domain
 286 size, TC intensity increases dramatically even though the environmental soundings are kept the
 287 same (see details in the Appendix). Consistent with this, Yang et al (2007) showed in both 2D and
 288 3D numerical experiments maximum wind speeds exceeding PI by more than 20 m/s. Wang and Xu
 289 (2010) found that maximum azimuthal averaged wind from a 3D integration may be about 25-40%
 290 stronger than PI. They suggested that lateral energy transport contributes significantly to local
 291 energy balance in the eyewall, and that the local energy balance may be of limited use.

292 To assess the flow imbalance, we compute V_g as a surrogate for azimuthal gradient wind:

$$293 \quad \frac{V_g^2}{r} + fr = -\frac{1}{\rho} \frac{\partial p}{\partial r}, \quad (3)$$

294 where r is the radius, p is the pressure, ρ is the density, and, f is the Coriolis parameter. Figure 5
 295 shows the radial distribution of both simulated tangential wind and gradient wind V_g averaged from
 296 days 3.75 to 5, at the height of the maximum wind speed (~ 1.3 km). In contrast to V_{max} , the
 297 maximum value of V_g is ~ 85 m/s and located at approximately 50 km, while V_g is ~ 75 m/s at the
 298 RMW (as defined by the actual wind). This indicates that super-gradient effects are largely
 299 responsible for the discrepancies between PI and V_{max} , which is close to PI (~ 80 m/s, see Fig. 2b and
 300 Table 2), if we use the environmental value of $C_k/C_d \sim 0.9$.

301 One can further assess the momentum balance in the radial direction. In a quasi-steady state,
 302 the equation for the radial momentum in an inviscid flow may be written in cylindrical coordinates
 303 as:

$$304 \quad \overline{u \frac{\partial u}{\partial r}} + \frac{\overline{v \partial u}}{r \partial \theta} + \overline{w \frac{\partial u}{\partial z}} = \frac{\overline{v^2}}{r} - \frac{\overline{v_g^2}}{r} \quad (4),$$

305 where u , v , and w are radial, azimuthal, and vertical winds, respectively, and the overbars denote
 306 azimuthal and temporal averages. Each term in equation (4) is evaluated using the model output at

307 1.3 km. Figure 5b shows that the right hand side of Equation (4), a measure of the degree of
308 departure from gradient wind balance, is $\sim 0.18 \text{ m/s}^2$ at RMW, and largely balanced by the
309 momentum transport of the vertical advection ($\sim 0.15 \text{ m/s}^2$). The gradient wind imbalance might be
310 incorporated in the PI theory, as discussed in Bryan and Rotunno (2009), who find that the PI theory
311 with this modification is useful for explaining the difference between PI and the axisymmetric
312 model simulated maximum azimuthal wind speed. Nevertheless, this appears to be insufficient for
313 explaining the difference in the gradient wind between the 3D experiments and PI.

314 **3.2.3 TC intensity as a function of T_o**

315 Figure 6 shows the time series of the minimum sea level pressure and the maximum
316 azimuthal mean wind for the experiments in which T_o increases from 195 K to 215 K. The
317 minimum sea level pressure reaches its minimum around day 4 and persists for about 1 to 1.5 days,
318 in the range 885hPa to 910hPa for all the experiments during this period, and increases afterwards
319 as the TCs weaken. One exception is that the TC at $T_o = 195 \text{ K}$ cannot maintain its peak intensity,
320 weakening immediately after reaching peak intensity. The intensities of these transient TC solutions,
321 as measured by minimum sea level pressure, increase with colder tropopause temperature, by ~ 1
322 hPa per degree cooling.

323 The time series of the maximum azimuthal wind speed (Figure 6b) show maximum values
324 from 95 to 102 m/s, reached between day 3.75 and 5. Unlike the minimum sea level pressure, the
325 azimuthal wind is subject to aliasing error in the conversion from Cartesian to cylindrical
326 coordinates. Figure 7 shows the maximum azimuthal wind (V_{max}) versus T_o for all the experiments
327 with 4 km horizontal grid spacing, over three different values of SST: 26, 28 and 30°C. The impact
328 of the tropopause temperature on the TC at each SST is evident. Taking all these experiment
329 together, linear regression yields a 0.46 m/s increase of maximum azimuthal wind for every degree
330 cooling at the tropopause. The maximum gradient wind, as discussed previously, is weaker, $\sim 70\%$

331 of the maximum azimuthal wind in all the experiments. Figure 7b shows that the peak gradient wind
332 from each experiment scales similarly to the actual wind with T_o .

333 **3.2.4. Sensitivity to resolution**

334 In this subsection, we examine the sensitivity of our TC solutions, including TC intensity
335 and its dependence on the tropopause temperature, to horizontal resolution. In this set of
336 experiments, we use 8 km horizontal grid spacing in the inner domain and 24 km in the outer
337 domain, while keeping the same domain size and physical parameterization schemes. The
338 environmental soundings are generated from RCE integrations at $Dx = 8$ km, which yields similar
339 $PI - T_o$ slope, ~ 0.4 m/s/K (black squares in Figure 3).

340 As the grid spacing increases from 4 km to 8 km, TC intensity decreases, as expected. For
341 example, the maximum wind speed at $T_o = 200$ K decreases from 105 m/s with $Dx = 4$ km to 90 m/s
342 with $Dx = 8$ km and $SST = 28^\circ\text{C}$. Figure 7 shows simulated maximum azimuthally averaged wind
343 speed as a function of outflow temperature. The slope between hurricane intensity and T_o increases
344 slightly to ~ 0.5 m/s/K.

345 **4. TCs in statistical equilibrium**

346 In this section, we examine TC intensity in equilibrium states. We perform five convective-
347 permitting experiments with the same range of values for the tropopause temperature parameter T_o :
348 195, 200, 205, 210, and 215 K. In order to reduce computation cost, we use a smaller domain size
349 (3200 km) with double periodic lateral boundary conditions and $Dx = 8$ km, but we keep the same
350 physics and the number of vertical levels as in the previous experiments. Using lower horizontal
351 resolution $Dx = 8$ km may be justified by the fact that the model still produces a similar relation
352 between the tropopause temperature and TC intensity as that obtained with $Dx = 4$ km, although the
353 simulated TC intensities overall are reduced. We do not use the nesting technique in these long
354 integrations. The model is integrated for 200 days to obtain adequate statistics of TC intensity in the
355 equilibrium state. In RCE, some aspects of the model solutions are well constrained, e.g., the time

356 and domain averaged rainfall equals the evaporation, as required by the equilibrium water vapor
357 budget, and the vertically-integrated radiative cooling is in balance with the net surface enthalpy
358 flux due to the conservation of moist static energy. In these experiments, both the domain averaged
359 evaporation and rainfall are ~ 4.1 mm/day, and vary by about 10% in its time mean with respect to
360 the increases of radiative cooling in these RCE states.

361 Figure 9 displays the time series of both the minimum sea level pressure and maximum
362 azimuthal mean wind speed. During the first 10 days, the maximum azimuthal wind speed varies
363 between 80 and 90 m/s. The peak intensities of these TCs also scale similarly with T_o , consistent
364 with previous results. After this first peak, the TCs weaken substantially but maintain coherent
365 axisymmetric structures. It is also evident in Figure 9a that a colder tropopause not only yields
366 larger intensities (e.g., in the first 10 days), but also larger temporal oscillations throughout the first
367 100 days. The strengthening-weakening cycle repeats a few times before a statistical equilibrium is
368 established.

369 During this transition stage, the free tropospheric temperature warms by several K (not
370 shown) in the TC-RCE state over that in the pure RCE state, indicating that the environment has
371 been substantially modified by the presence of TCs. After approximately 100 days (similar to the
372 time scale to reach the original RCE), the model solution eventually settles into a statistical
373 equilibrium. In this equilibrium the TC intensities, measured in either pressure or winds, oscillate
374 irregularly. Similar oscillatory behavior of statistically steady TC solutions has been noted in other
375 axisymmetric modeling studies (e.g., Hakim 2011).

376 Because of the temporal oscillations, it is not immediately clear if the intensity of these TCs
377 scales with the tropopause temperature similarly to the transient solutions in the first 10 days. Here
378 we use two metrics to quantify TC intensity: the time mean and the 99% quantile of maximum wind

379 speed. Both are computed from the last 100 days of the integrations, after the initial large
380 oscillations have settled down.

381 The relationship between equilibrium TC intensity and tropopause temperature is shown in
382 Figure 10 for these five equilibrium experiments. Both the mean intensity and the 99% quantile
383 show a strong relationship with the tropopause temperature. The standard deviation of the mean
384 intensity generally increases with a colder tropopause, although the minimum occurs at $T_o=200$ K.
385 The coefficient obtained from linear regression is ~ -0.48 m/s/K for the mean intensity, and ~ -0.67
386 m/s/K for the 99% quantile. This is slightly larger than the values found in the transient TC
387 solutions, and still at the low end of the PI's dependence on tropopause temperature.

388 **5. Conclusions**

389 We have investigated the impact of the tropopause temperature on the intensity of idealized TCs
390 using a 3D mesoscale model in a radiative-convective environment. While the model has “full
391 physics” in all other respects, the radiative cooling is specified to a constant 1.2 K/day in the
392 troposphere, as well as a relaxation to constant tropopause temperature in an isothermal stratosphere.
393 That imposed tropopause and stratospheric temperature is used as our control parameter, and varied
394 over a range of 40K.

395 The potential intensity, calculated using the thermodynamic profiles that are simulated in
396 the small domain in the radiative-convective equilibrium before the TCs are introduced, yields an
397 increase of 0.4 to 1 m/s for each degree cooling at the tropopause. The specific value within this
398 range depends on several parameters in the PI code; with the ratio of exchange coefficients being
399 the most important of those. 3D integrations using the WRF model with horizontal grid spacing 4
400 km yield intense tropical cyclones with maximum azimuthal wind speed exceeding PI by substantial
401 fractions; the magnitude of these excesses are also dependent on the parameters chosen in the PI
402 calculation. Some of this discrepancy is explained by the super-gradient wind. On the other hand,

403 the intensity of these 3D TCs show a ~ 0.4 m/s increase with one degree decrease at the tropopause
404 in the radiative-convective equilibrium. This value is near the lower end of the PI estimated TC
405 intensity dependence. Sensitivity experiments with horizontal grid spacing of 8 km produce less
406 intense TCs, as expected, but a similar slope (~ 0.5 m/s/K) with respect to the tropopause
407 temperature.

408 Equilibrium TC solutions are obtained in five 200-day experiments, over a range of
409 tropopause temperatures 20K wide, with horizontal grid spacing of 8 km in a 3200-km-wide
410 numerical domain. These equilibrium TC solutions have maximum wind speeds in the range 40 - 60
411 m/s and minimum sea level pressures in the range 940 - 970 hPa, and exhibit significant temporal
412 viability. When the TC intensity in these solutions is measured using either the time mean or the
413 99% quantile of maximum wind speed, both quantities show a strong relationship with the
414 tropopause temperature. The linear regression coefficient is ~ 0.48 m/s/K for the mean intensity,
415 and ~ 0.67 m/s/K for the 99% quantile of the maximum wind speed. A colder tropopause not only
416 yields more intense TCs, but also leads to larger temporal variability in the TC intensity.

417 In summary, this study shows that both the potential intensity theory and the 3D WRF
418 numerical modeling are qualitatively consistent on the impact of the environmental tropopause
419 temperature upon the intensity of idealized TCs, while this TC-tropopause temperature relationship
420 is quantitatively weaker in the 3D modeling. The quantitative discrepancy may be attributed to
421 several factors yet to be considered in the PI theory on the one hand, and to the inherent
422 uncertainties in the numerical modeling on the other. Future improvement in both theory and
423 modeling will be crucial for better understanding and quantification of the TC activities and their
424 dependence on the environmental conditions.

425

426 **Appendix: Domain size dependence of hurricane intensity**

427
428 The size of the outer domain is 6000 km in the nesting experiments, and 3200 km in the statistical
429 equilibrium integrations. Domain size can influence TC intensity, as found previously in
430 axisymmetric models (Chavas and Emanuel 2013). We have experimented different domain size for
431 the experiment with $SST=28^{\circ}C$ and $T_o=205K$. We performed experiments varying the size of the
432 outer domain from 1800, 3000, to 6000 km, keeping the inner domain the same. In one additional
433 experiment, only the inner domain (1200 km) is used. Figure A1 shows that the TC peak intensity in
434 the 3000 km and 6000 km experiments is of the same magnitude, but the latter shows more
435 temporal viability. The maximum wind speed is reduced to to 90 m/s in the 1800 km experiment,
436 and 80 m/s in the smallest domain (1200 km) experiment. The time to achieve peak intensity is also
437 delayed.

438 **Acknowledgement**

439
440 This work is supported by NOAA grants NA08OAR4320912, NA11OAR4310093, and NSF grants
441 AGS 1143959. We are thankful to Dr. Kerry Emanuel for sharing his PI code. We thank NCAR's
442 computational and Information Systems Laboratory, where part of model integrations were performed. We
443 also thank Dr. Gustavo J. P. Correa for maintaining the Linux cluster where some of model integrations were
444 performed.

445

446 **Reference**

- 447 Bell, M. M., M. T. Montgomery, K. A. Emanuel, 2012: Air–Sea Enthalpy and Momentum
448 Exchange at Major Hurricane Wind Speeds Observed during CBLAST. *J. Atmos. Sci.*, **69**, 3197–
449 3222.
- 450 Bister, M., and K.A. Emanuel, 1997: The genesis of Hurricane Guillermo: TEXMEX analyses and a
451 modeling study. *Mon. Wea. Rev.*, **125**, 2662–2682.
- 452 Bister, M., and K. A. Emanuel, 2002: Low frequency variability of tropical cyclone potential
453 intensity, I, Interannual to interdecadal variability. *J. Geophys. Res.*, **107**, 4801,
454 doi:10.1029/2001JD000776.
- 455 Black, P. G., and Coauthors, 2007: Air–sea exchange in hurricanes: Synthesis of observations from
456 the Coupled Boundary Layer Air–Sea Transfer experiment. *Bull. Amer. Meteor. Soc.*, **88**, 357–374.
- 457 Braun, S. A., W-K Tao, 2000: Sensitivity of High-Resolution Simulations of Hurricane Bob (1991)
458 to Planetary Boundary Layer Parameterizations. *Mon. Wea. Rev.*, **128**, 3941–3961.
- 459 Bryan, George H., 2012: Effects of Surface Exchange Coefficients and Turbulence Length Scales
460 on the Intensity and Structure of Numerically Simulated Hurricanes. *Mon. Wea. Rev.*, **140**, 1125–
461 1143.
- 462 Bryan, G. H., and R. Rotunno, 2009a: Evaluation of an Analytical Model for the Maximum
463 Intensity of Tropical Cyclones. *J. Atmos. Sci.*, **66**, 3042–3060.
- 464 Bryan, G. H., and R. Rotunno, 2009b: The Maximum Intensity of Tropical Cyclones in
465 Axisymmetric Numerical Model Simulations. *Mon. Wea. Rev.*, **137**, 1770–1789.
- 466 Chavas, D. R., and K. A. Emanuel, 2014: Quasi-steady tropical cyclone structure in axisymmetric
467 radiative-convective equilibrium. In review.
- 468 Chen, S.-H., and W.-Y. Sun (2002), A one-dimensional time dependent cloud model, *J. Meteorol.*
469 *Soc. Jpn.*, **80**, 99–118.
- 470 Craig, G. C., and S. L. Gray, 1996: CISK or WISHE as the Mechanism for Tropical Cyclone
471 Intensification. *J. Atmos. Sci.*, **53**, 3528–3540. doi: [http://dx.doi.org/10.1175/1520-
472 0469\(1996\)053<3528:COWATM>2.0.CO;2](http://dx.doi.org/10.1175/1520-0469(1996)053<3528:COWATM>2.0.CO;2)
- 473 Emanuel, K., 2010: Tropical Cyclone Activity Downscaled from NOAA-CIRES Reanalysis, 1908–
474 1958. *J. Adv. Model. Earth Syst.*, **2**, doi:10.3894/JAMES.2010.2.1.
- 475 Emanuel, K., and R. Rotunno, 2011: Self-Stratification of Tropical Cyclone Outflow. Part I:
476 Implications for Storm Structure. *J. Atmos. Sci.*, **68**, 2236–2249.
- 477 Emanuel, K., S. Solomon, S., D. Folini, S. Davis, and C. Cagnazzo, 2013: Influence of tropical
478 tropopause layer cooling on Atlantic hurricane activity. *J. Clim.*, **26**, 2288–2301.
- 479 Montgomery, M. T., M. E. Nicholls, T. A. Cram, A. B. Saunders, 2006: A Vortical Hot Tower
480 Route to Tropical Cyclogenesis. *J. Atmos. Sci.*, **63**, 355–386.
- 481 Hakim, G. J., 2011: The Mean State of Axisymmetric Hurricanes in Statistical Equilibrium. *J.*
482 *Atmos. Sci.*, **68**, 1364–1376. doi: <http://dx.doi.org/10.1175/2010JAS3644.1>
- 483 Haus, B. K., D. Jeong, M. A. Donelan, J. A. Zhang, and I. Savelyev, 2010: Relative rates of sea–air
484 heat transfer and frictional drag in very high winds. *Geophys. Res. Lett.*, **37**, L07802,
485 doi:10.1029/2009GL042206.

486 Hausman, S.A., K.V. Ooyama, W.H. Schubert, 2006: Potential Vorticity Structure of Simulated
487 Hurricanes. *J. Atmos. Sci.*, **63**, 87–108.

488 Hong, S.-Y., Y. Noh, J. Dudhia, 2006: A New Vertical Diffusion Package with an Explicit
489 Treatment of Entrainment Processes. *Mon. Wea. Rev.*, **134**, 2318–2341.

490 Kepert, J. D., 2001: The dynamics of boundary layer jets within the tropical cyclone core. Part I:
491 Linear theory. *J. Atmos. Sci.*, **58**, 2469–2484.

492 Kepert, J. D., 2012: Choosing a Boundary Layer Parameterization for Tropical Cyclone
493 Modeling. *Mon. Wea. Rev.*, **140**, 1427–1445. doi: <http://dx.doi.org/10.1175/MWR-D-11-00217.1>

494 Klemp, J. B., J. Dudhia, A. D. Hassiotis (2008), An upper gravity-wave absorbing layer for NWP
495 Applications, *Mon. Wea. Rev.*, *136*, 3987–4004.

496 Knutson, T.R., R.E. Tuleya, J. J. Sirutis, G. A. Vecchi, and I. Held, 2008: Simulated reduction in
497 Atlantic hurricane frequency under twenty-first- century warming conditions. *Nat. Geosci.*, **1**(6),
498 359–364.

499 Kossin, J. P., and S. J. Camargo, 2009: Hurricane track variability and secular potential intensity
500 trends. *Climatic Change*, **97**, 329–337, DOI:10.1007/s10584-009-9748-2.

501 Lin, I.-I., P. Black, J. F. Price, C.-Y. Yang, S. S. Chen, C.-C. Lien, P. Harr, N.-H. Chi, C.-C. Wu,
502 and E. A. D'Asaro (2013), An ocean coupling potential intensity index for tropical
503 cyclones, *Geophys. Res. Lett.*, **40**, 1878–1882, doi:[10.1002/grl.50091](https://doi.org/10.1002/grl.50091).

504 Lin, Y.-L., R. D. Farley, and H. D. Orville (1983), Bulk parameterization of the snow field in a
505 cloud model, *J. Clim. Appl. Meteorol.*, *22*, 1065–1092.

506 Montgomery, M. T., and R. K. Smith, 2011: Paradigms for tropical-cyclone intensification. *Quart. J.*
507 *Roy. Meteor. Soc.*, **137**, 1–31 Mrowiec, A., S.T. Garner, O.M. Pauluis, 2011: Axisymmetric
508 Hurricane in a Dry Atmosphere: Theoretical Framework and Numerical Experiments. *J. Atmos.*
509 *Sci.*, **68**, 1607–1619.

510 Nolan, D. S., J. A. Zhang, D. P. Stern, 2009: Evaluation of Planetary Boundary Layer
511 Parameterizations in Tropical Cyclones by Comparison of In Situ Observations and High-
512 Resolution Simulations of Hurricane Isabel (2003). Part I: Initialization, Maximum Winds, and the
513 Outer-Core Boundary Layer. *Mon. Wea. Rev.*, **137**, 3651–3674.

514 Nolan, D. S., D. P. Stern, J. A. Zhang, 2009: Evaluation of Planetary Boundary Layer
515 Parameterizations in Tropical Cyclones by Comparison of In Situ Observations and High-
516 Resolution Simulations of Hurricane Isabel (2003). Part II: Inner-Core Boundary Layer and Eyewall
517 Structure. *Mon. Wea. Rev.*, **137**, 3675–3698.

518 Nolan, D. S., E. D. Rappin, and K. A. Emanuel, 2007: Tropical cyclogenesis sensitivity to
519 environmental parameters in radiative–convective equilibrium. *Quart. J. Roy. Meteor. Soc.*, **133**,
520 2085–2107.

521 Ooyama, K., 1969: Numerical Simulation of the Life Cycle of Tropical Cyclones. *J. Atmos. Sci.*, **26**,
522 3–40.

523 Pauluis, O., S. Garner, 2006: Sensitivity of Radiative–Convective Equilibrium Simulations to
524 Horizontal Resolution. *J. Atmos. Sci.*, **63**, 1910–1923.

525 Persing, J., M. T. Montgomery, 2003: Hurricane Superintensity. *J. Atmos. Sci.*, **60**, 2349–2371.

526 Persing, J., Montgomery, M. T., McWilliams, J. C., and Smith, R. K.: Asymmetric and
527 axisymmetric dynamics of tropical cyclones, *Atmos. Chem. Phys. Discuss.*, 13, 13323-13438,
528 doi:10.5194/acpd-13-13323-2013, 2013.

529 Ramsay, H. A., and A. H. Sobel, 2011: Effects of relative and absolute sea surface temperature on
530 tropical cyclone potential intensity using a single-column model. *J. Climate*, **24**, 183–193.

531 Ramsay, H., 2013: The effects of imposed stratospheric cooling on the maximum intensity of
532 tropical cyclones in axisymmetric radiative-convective equilibrium. *J. Climate*, In press.

533 Randel, W. J., et al. (2009), An update of observed stratospheric temperature trends, *J. Geophys.*
534 *Res.*, 114, D02107, doi:10.1029/2008JD010421.

535 Rappin, E. D., D. S. Nolan, and K. A. Emanuel, 2010: Thermodynamic control of tropical
536 cyclogenesis in environments of radiative-convective equilibrium with shear. *Quart. J. Roy.*
537 *Meteorol. Soc.*, 136, 1954-1971.

538 Raymond, D. J., S. Sessions, and Z. Fuchs, 2007: A theory for the spinup of tropical depressions,
539 *Quart. J. Roy. Meteorol. Soc.*, 133, 1743-1754.

540 Rotunno, R., and G. H. Bryan, 2012: Effects of parameterized diffusion on simulated hurricanes. *J.*
541 *Atmos. Sci.*, **69**, 2284-2299, doi:10.1175/JAS-D-11-0204.1

542 Rotunno, R., and K.A. Emanuel, 1987: An air-sea interaction theory for tropical cyclones, Part II:
543 Evolutionary study using axisymmetric nonhydrostatic numerical model. *J. Atmos. Sci.*, **44**, 542-
544 561.

545 Skamarock, W. C., J. B. Klemp, J. Dudhia, D. O. Gill, D. M. Barker, M. G. Duda, X. Huang, W.
546 Wang, and J. G. Powers (2008), A description of the Advanced Research WRF version 3, *NCAR*
547 *Tech. Note NCAR/TN-475+STR*, 125 pp.

548 Smith, R.K., S. Vogl, 2008. A simple model of the hurricane boundary layer revisited. *Q. J. R.*
549 *Meteorol. Soc.* **134**: 337–351.

550 Smith, R. K., Montgomery, M. T. and Vogl, S. (2008), A critique of Emanuel's hurricane model and
551 potential intensity theory. *Q.J.R. Meteorol. Soc.*, 134: 551–561. doi: 10.1002/qj.241

552 Smith, R. K. and Montgomery, M. T. (2010), Hurricane boundary-layer theory. *Q.J.R. Meteorol.*
553 *Soc.*, 136: 1665–1670. doi: 10.1002/qj.679

554 Tang, B., and K. Emanuel, 2010: Midlevel ventilation's constraint on tropical cyclone intensity. *J.*
555 *Atmos. Sci.*, **67**, 1817-1830.

556 Tang, B., and K. Emanuel, 2012: Sensitivity of tropical cyclone intensity to ventilation in an
557 axisymmetric model. *J. Atmos. Sci.*, **69**, 2394-2413.

558 Troen, I., and L. Mahrt (1986), A simple model of the atmospheric boundary layer: Sensitivity to
559 surface evaporation, *Boundary Layer Meteorol.*, 37, 129–148.

560 Zhang, D-L, E. Altshuler, 1999: The Effects of Dissipative Heating on Hurricane Intensity. *Mon.*
561 *Wea. Rev.*, **127**, 3032–3038.

562 Zhang, D.-L., and H. Chen (2012), Importance of the upper-level warm core in the rapid
563 intensification of a tropical cyclone, *Geophys. Res. Lett.*, 39, L02806, doi:10.1029/2011GL050578

564 Zhang, J. A., 2010: Estimation of dissipative heating using low-level in situ aircraft observations in
565 the hurricane boundary layer. *J. Atmos. Sci.*, **67**, 1853–1862.

566 Zhang, J. A., P. Zhu, F. J. Masters, R. F. Rogers, F. D. Marks, 2011: On Momentum Transport and
567 Dissipative Heating during Hurricane Landfalls. *J. Atmos. Sci.*, **68**, 1397–1404.

568 Zhao, M., and I. M. Held, 2012: TC-permitting GCM simulations of hurricane frequency response
569 to sea surface temperature anomalies projected for the late 21st century. *J. Climate*, **25**(8),
570 doi:10.1175/JCLI-D-11-00313.1.

571 Zhao, M., and I. M. Held, S.-J. Lin, and G. A. Vecchi, 2009: Simulations of global hurricane
572 climatology, interannual variability, and response to global warming using a 50-21 km resolution
573 GCM. *J. Climate*, **22**, 6653–6678.

574 Yang, B, Y. Wang, and B Wang, 2007: The Effect of Internally Generated Inner-Core Asymmetries
575 on Tropical Cyclone Potential Intensity. *J. Atmos. Sci.*, **64**, 1165–1188.

576 Wang, Y, and J Xu, 2010: Energy Production, Frictional Dissipation, and Maximum Intensity of a
577 Numerically Simulated Tropical Cyclone. *J. Atmos. Sci.*, **67**, 97–116.

578 Wing, A.A, A.H. Sobel, and S.J. Camargo, 2007. The relationship between the potential and actual
579 intensities of tropical cyclones on interannual time scales. *Geophysical Research*
580 *Letters*, 34, L08810

581 Vecchi, G. A., and B. J. Soden, 2007: Effect of remote sea surface temperature change on tropical
582 cyclone potential intensity. *Nature*, **450**, 1066–1071.

583 Vecchi, G. A., S. Fueglistaler, I. M. Held, T. R. Knutson, and M. Zhao, 2013: Impacts of
584 Atmospheric Temperature Trends on Tropical Cyclone Activity. *J. Climate*, **26**, 3877–3891.

585

586 **Table 1** Three-dimensional RCE and TC experiments

587

RCE experiments	$T_0=195, 200, 205, 210, 215$ K. SST= $26, 28, \text{ and } 30^\circ$ C. $Dx = 4$ km $T_0=195, 200, 205, 210, 215$ K. SST= 28° C. $Dx = 8$ km Small domain (200 km)
Transient TC experiments	$T_0=195, 200, 205, 210, 215$ K. SST= $26, 28, \text{ and } 30^\circ$ C. $Dx = 4$ km $T_0=195, 200, 205, 210, 215$ K. SST= 28° C. $Dx = 8$ km Two nest grids: 6,000 km for the outer domain, and 1,200 km for the inner domain.
Equilibrium TC experiments	$T_0=195, 200, 205, 210, 215$ K. SST= 28° C. $Dx = 8$ km. Single domain (3,000 km).

588

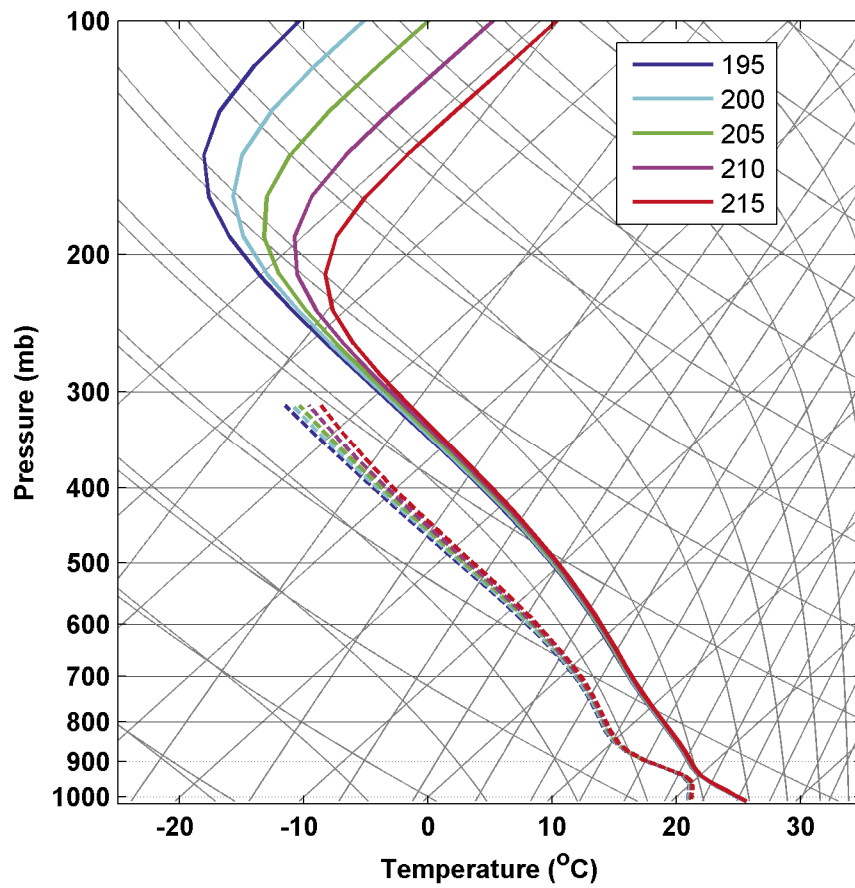
589

590 **Table 2.** Dependence of PI on the outflow temperature with different of choices of thermodynamics,
 591 C_k/C_d , and dissipative heating, computed from the small domain RCE soundings. The number in the
 592 parentheses is the PI value (m/s) for the case SST = 28°C and $T_o = 205$ K. Units for the two numbers
 593 are m/s/K and m/s, respectively. Bold values are the case for Figure 2.

594

C_k/C_d	Reversible thermodynamics		Pseudo-adiabatic thermodynamics	
	Dissipative heating off	Dissipative heating on	Dissipative heating off	Dissipative heating on
0.5	-0.41 (54)	-0.67 (66)	-0.43 (59)	-0.73 (72)
0.7	-0.49 (64)	-0.82 (78)	-0.53 (70)	-0.91 (86)
0.9	-0.57 (73)	-0.96 (89)	-0.62 (80)	-1.07 (99)

595



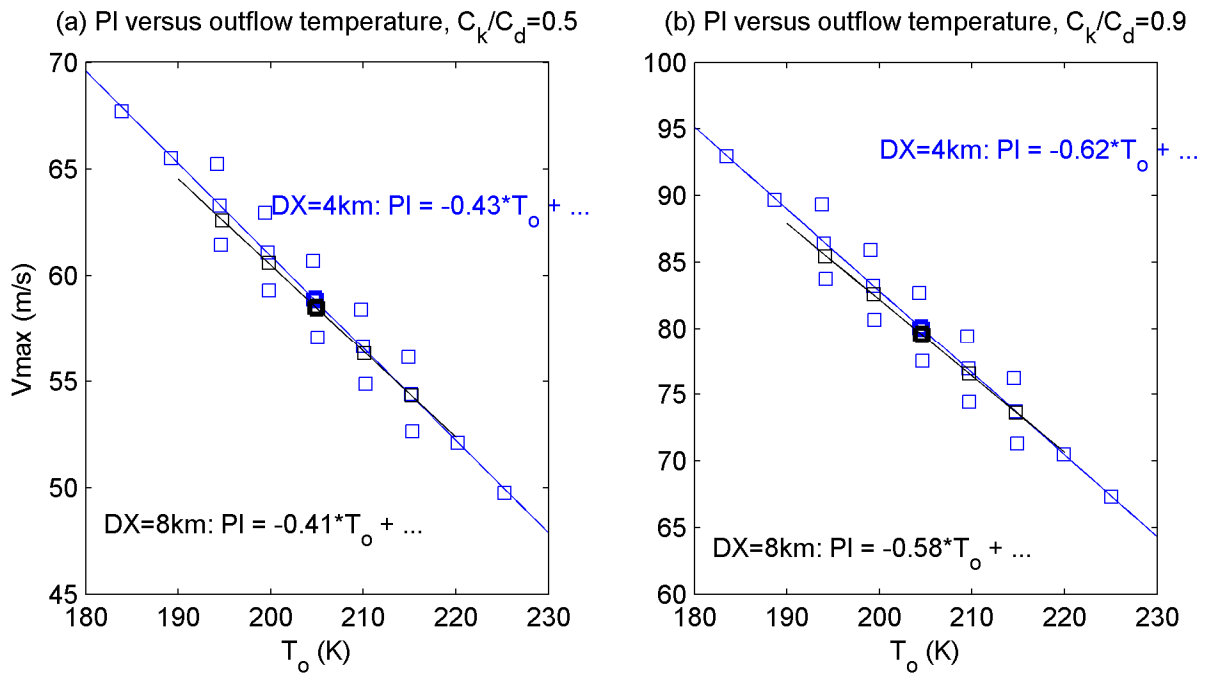
596

597 **Figure 1.** Skew-T Log-P diagram of the RCE soundings with five values of T_o at SST=28°C.

598

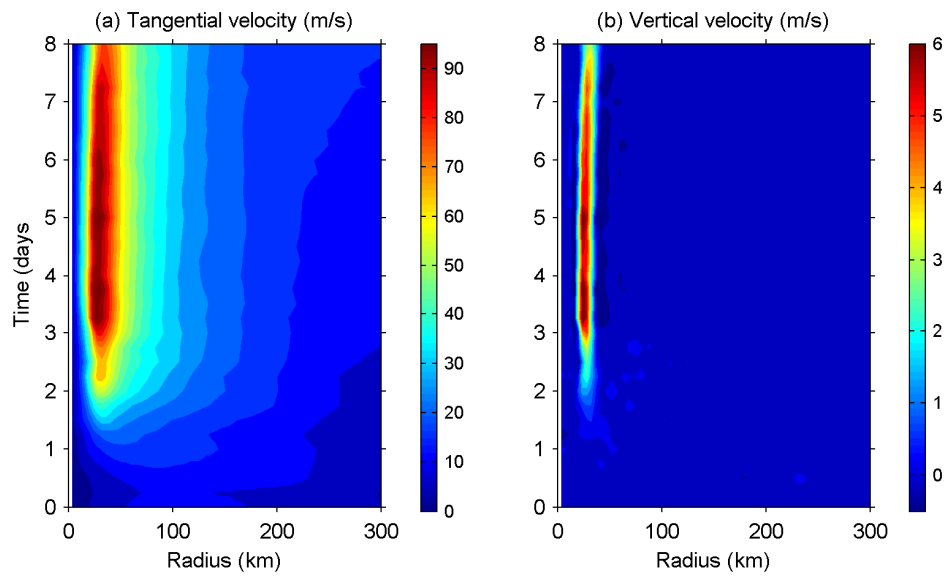
599

600



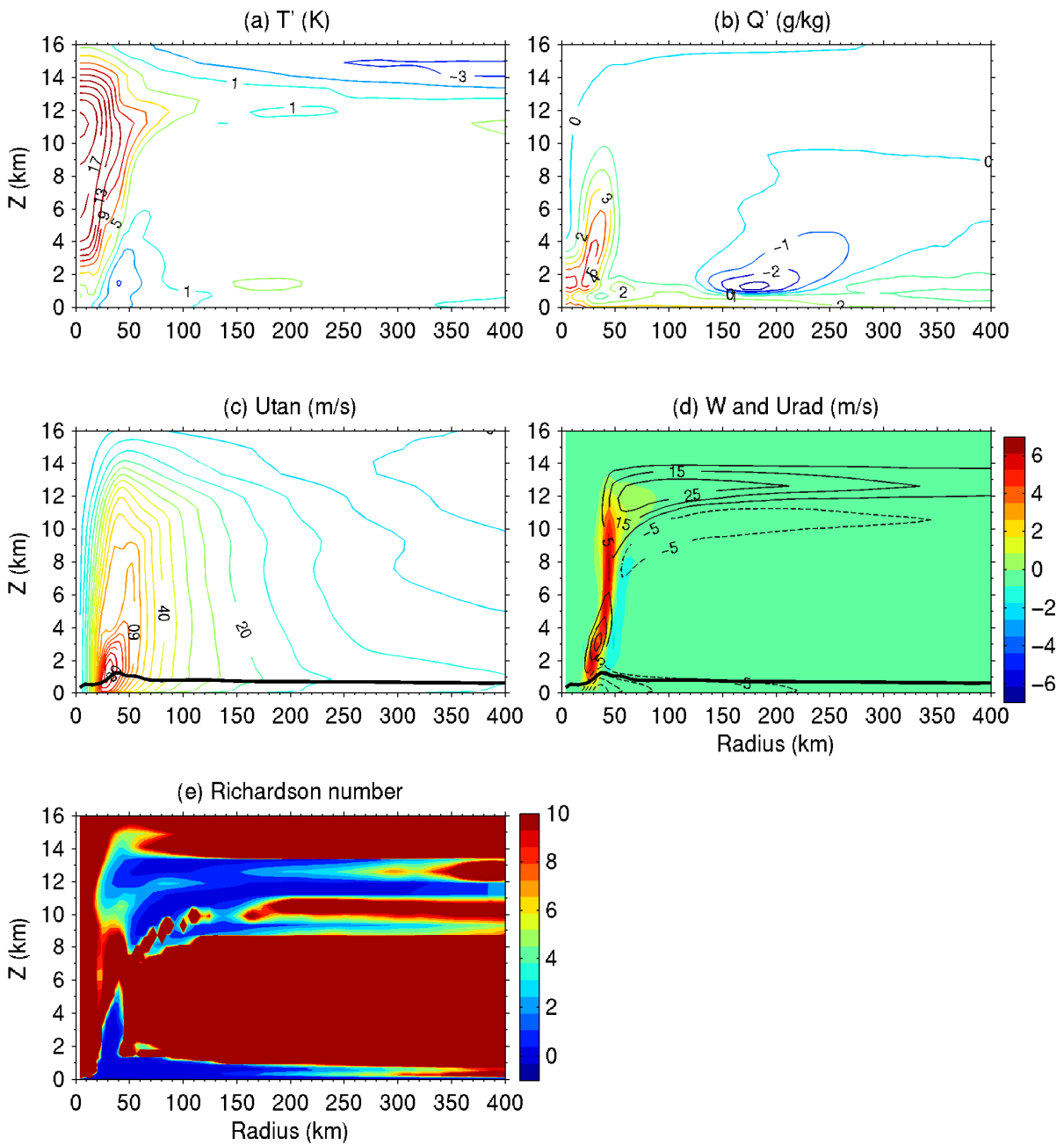
601
 602 **Figure 2.** Potential intensity as a function of the outflow temperature, both computed from
 603 Emanuel's PI code. Red squares denote those from 4-km small domain RCE integrations with three
 604 different values of SST: 26°C, 28°C, and 30°C, black squares denote those from 8-km small domain
 605 RCE integrations with SST = 28°C. Bold squares indicate results from the RCE sounding with SST
 606 = 28°C and $T_o = 205$ K.

607
 608
 609
 610



611

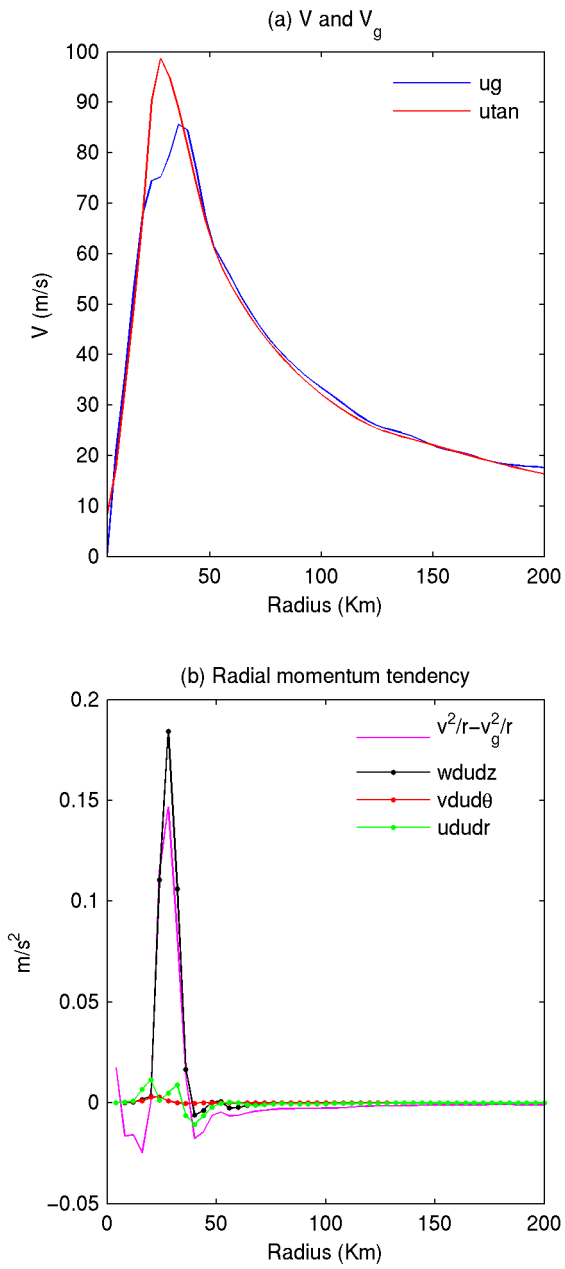
612 **Figure 3.** Time-radius diagram of (a) tangential wind speed (m/s), (b) vertical velocity (m/s) at the
613 level of maximum wind speed (~ 1.3 km) from the TC integration with $SST = 28^\circ\text{C}$ and $T_o = 205$ K.



614

615 **Figure 4.** Axisymmetric structure of the TCs with SST = 28°C and $T_o = 205$ K (a) temperature
 616 anomalies, (b) moisture anomalies, (c) tangential wind speed, (d) radial and vertical wind, and (e)
 617 Richardson number.

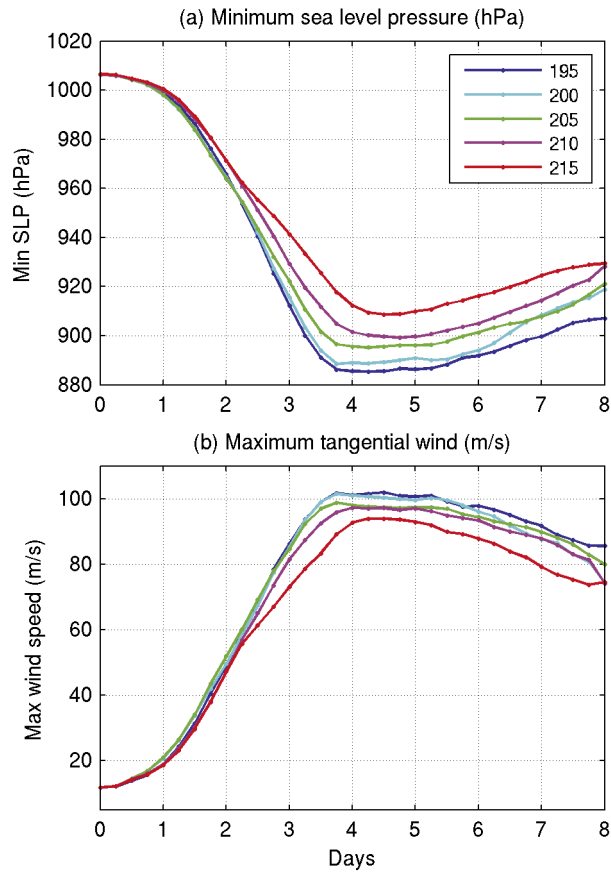
618



619

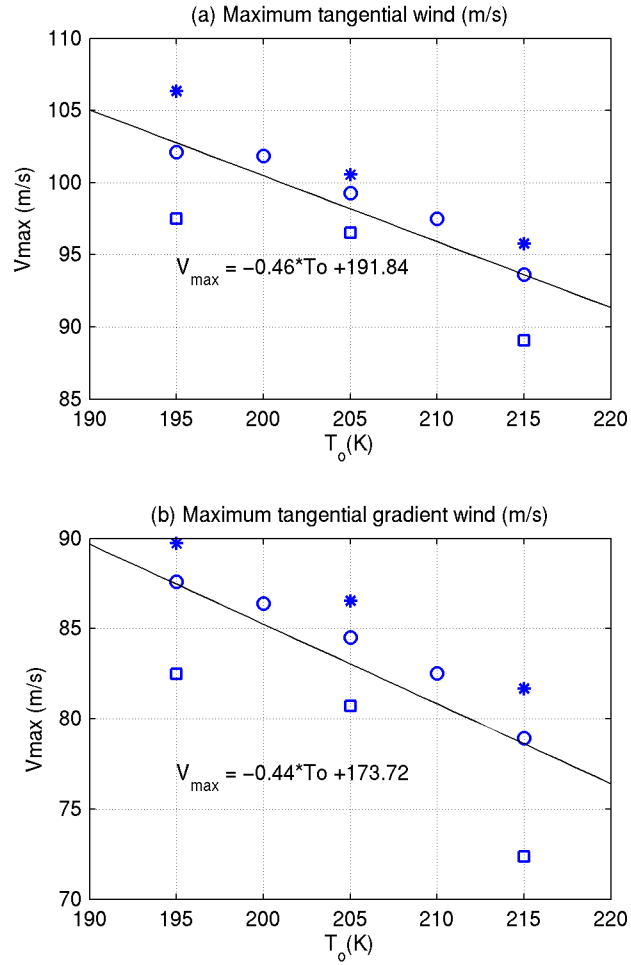
620 **Figure 5.** (a). Azimuthally averaged tangential wind (u_{tan}), and tangential gradient wind (u_g). (b)

621 Various terms in the equation (2) for the radial momentum.



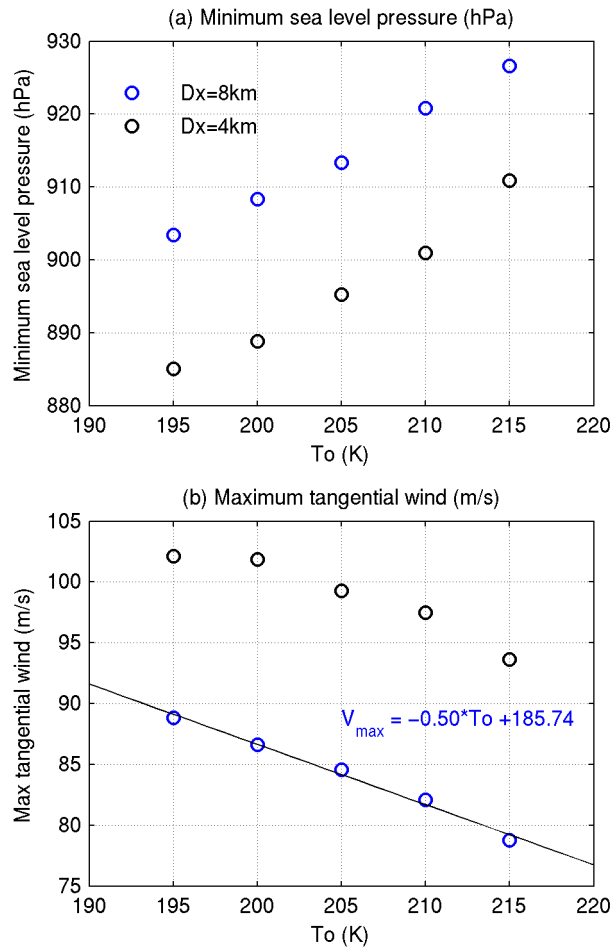
622

623 **Figure 6.** Time series of (a) minimum sea level pressure (hPa) and (b) maximum tangential wind
 624 speed (m/s) at $SST = 28^\circ C$ for five different values of $T_o = 195, 200, 205, 210,$ and 215 K. A three
 625 point smoothing is applied for all the time series.



626

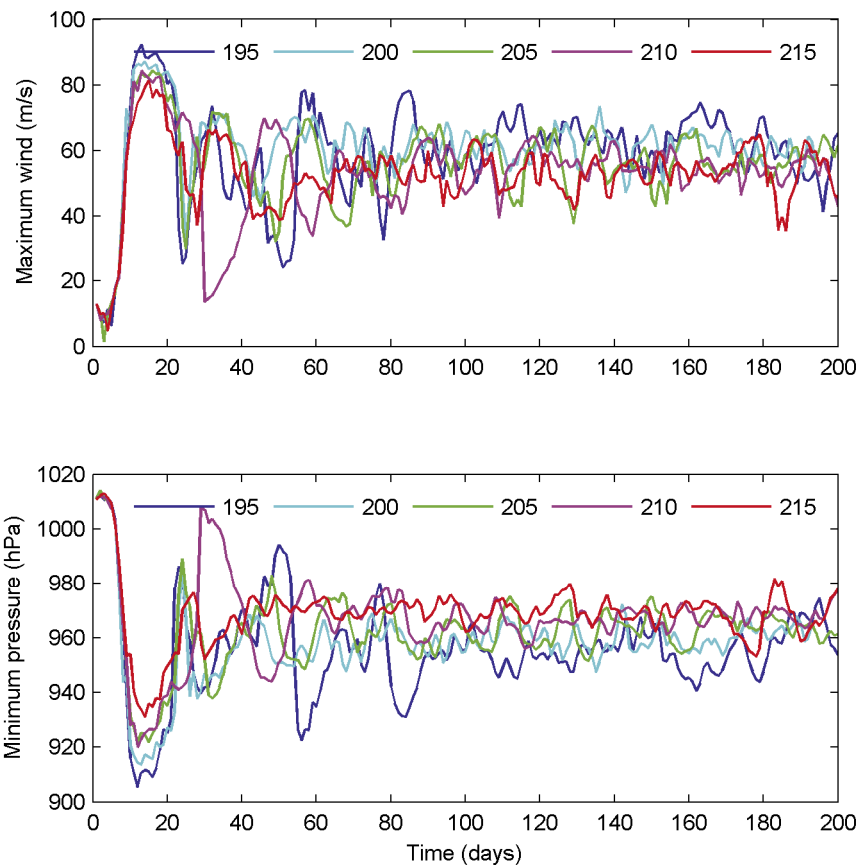
627 **Figure 7.** Time averaged maximum tangential wind and minimum SLP using 6 hourly model output
 628 from days 3.75 to 5. Squares denote SST = 26°C; circles, SST=28°C; and asterisks, SST=30°C.



629

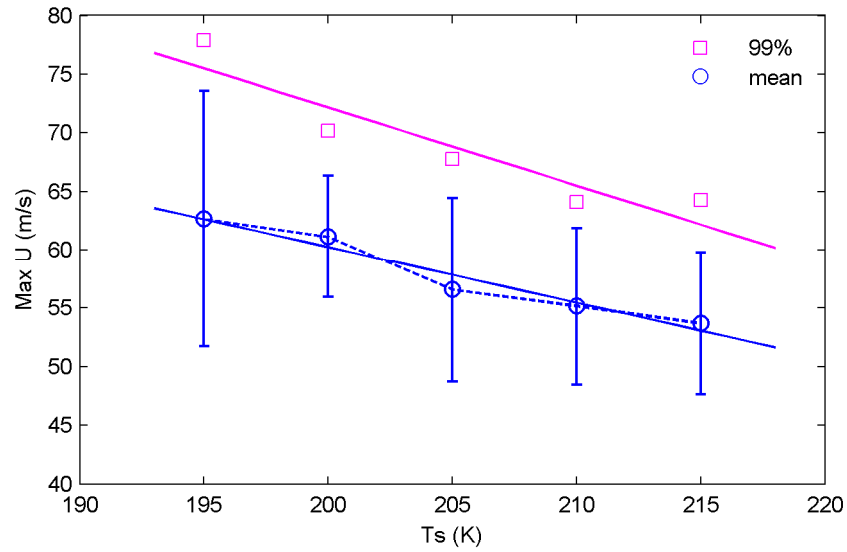
630 **Figure 8.** (a) Minimum sea level pressure and (b) maximum tangential wind speed from the
 631 experiments at SST=28°C, but with horizontal grid spacing Dx = 8 km (blue circles). Results from
 632 Dx = 4 km (black circles) are also shown for reference.

633



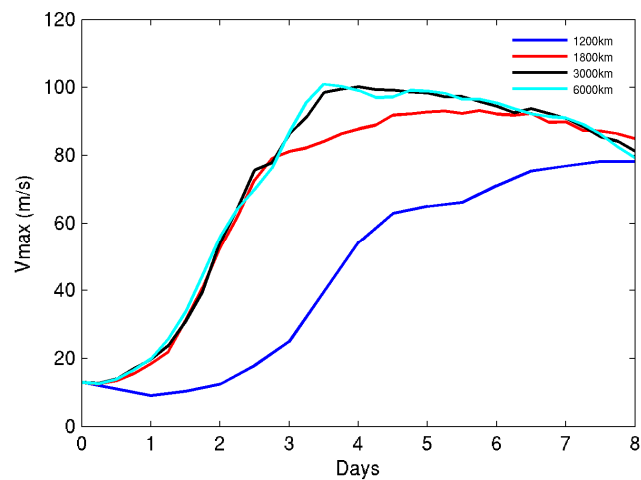
634

635 **Figure 9.** Maximum azimuthal mean winds (top panel) and minimum sea level pressure (bottom
636 panel) from five 200-day integrations.



638
 639 **Figure 10.** Maximum azimuthal mean wind from the last 100 days of the five experiments (Figure 9)
 640 versus T_o . The linear regression coefficient between V_{max} and T_o is ~ -0.48 m/s/K for the mean
 641 intensity (blue line), and ~ -0.67 m/s/K for the 99% quantile of the maximum wind speed (magenta
 642 line).

643



644

645 **Figure A1.** Maximum azimuthal mean tangential wind speed from 4 experiments with different
646 domain size: 1200, 1800, 3000, and 6000 km. Note that in the 1200-km integration, no nesting is
647 used.